INORGANIC CHEMISTRY FRONTIERS

RESEARCH ARTICLE

View Article Online
View Journal | View Issue

Cite this: *Inorg. Chem. Front.*, 2026, **13**, 4298

Engineering dimensionality and band-edges with lone-pair cations to achieve superior X-ray detection in metal-free perovskites

Jiasheng Gong,[a,b] Chensheng Lin, [a] Chunlei Yu,[a] Pengxiang Dong,[c] Tao Yan, [a] Huixin Fan*[a] and Min Luo *[a]

Metal-free perovskites (MFPs) have emerged as a promising class of environmentally friendly materials with exceptional optoelectronic properties, making them ideal candidates for X-ray detection and other applications. However, their development is often hindered by the trade-off between structural stability and electrical performance. In this work, we introduce a novel strategy that leverages the size effect and lone-pair electrons of the $N_2H_5^+$ cation to drive dimensionality reduction and band-edge optimization in MFPs. Using DABCO-$NH_4(BF_4)_3$ as a template, we successfully designed and synthesized a one-dimensional (1D) MFP, DABCO-$N_2H_5(BF_4)_3$, by introducing $N_2H_5^+$, which induced significant octahedral distortion and facilitated the transformation from a three-dimensional (3D) structure to a 1D perovskite framework. This 1D structure enhances anisotropic charge transport and optimizes the band-edge alignment, significantly improving electrical performance, while the organic cations in the 1D structure act as physical barriers, thereby improving stability. As a result, the DABCO-$N_2H_5(BF_4)_3$ SC device exhibits an ultrahigh sensitivity of 2570 μC Gy_{air}^{-1} cm^{-2} at 50 V, and an ultralow detection limit of 20.9 nGy_{air} s^{-1} along the parallel direction. This work presents a new design strategy for high-performance, environmentally friendly X-ray detectors, with enhanced sensitivity, lower detection limits, and high stability under various operational conditions.

Received 27th February 2026,
Accepted 28th March 2026

DOI: 10.1039/d6qi00393a

rsc.li/frontiers-inorganic

Introduction

Metal-free halide perovskites (MFHPs) represent a class of novel perovskite structures where toxic heavy metal ions in traditional metal halide perovskites (MHPs) are replaced by nitrogen-containing organic cations.[1–3] This approach has been heralded as a significant advancement in materials science, and it yields materials with outstanding optoelectronic properties while maintaining environmentally friendly processes.[4–7] Due to these outstanding characteristics, metal-free perovskites (MFPs) have found widespread applications in various fields, including ferroelectrics, dielectrics, X-ray detection and other fields.[8–12] Moreover, the fabrication of MFPs does not require toxic solvents, which enhances their biocompatibility and makes them an ideal candidate for green optoelectronic materials.[4,10,13,46] As a result, they have attracted substantial research interest as next-generation X-ray detection materials. However, despite the exceptional properties of MFPs, their development is hindered by a significant challenge, which is the trade-off between structural stability and electrical performance.[14] Similar to MHPs, halogen anions in MFHP crystal structures are prone to migration under external influence, which compromises the material's structural stability and subsequently affects the operational stability of the devices.[15] Furthermore, the electrical performance of MFPs is intrinsically related to charge collection efficiency, which is often constrained by the material's band structure and defect states.[16] Consequently, the materials struggle to simultaneously maintain structural stability while achieving high electrical performance.[17] Breaking the trade-off between stability and electrical performance of the MFPs and developing strategies which can synergistically achieve low detection limits and high sensitivity have become significant challenges in advancing high-performance and high stability MFP X-ray detection materials.

The use of pseudo-halogen anions to replace halide anions has been demonstrated as an effective strategy for enhancing structural stability and increasing the ion migration

[a]*State Key Laboratory of Functional Crystals and Devices, Fujian Institute of Research on the Structure of Matter, Chinese Academy of Sciences, Fuzhou, Fujian 350002, China. E-mail: lm8901@fjirsm.ac.cn, huixinfan@fjirsm.ac.cn*
[b]*Fujian College, University of Chinese Academy of Sciences, Fuzhou, Fujian 350002, China*
[c]*School of Materials Science and Engineering, Nankai University, Tianjin 300350, China*

barriers.[18,19] This approach has been shown to improve the structural stability of MFPs by enhancing hydrogen bonding interactions and creating a more rigid local coordination environment.[20] These interactions effectively suppress ion migrations and reduce the noise current in devices, which enhances the long-term operational stability of the MFPs.[21] However, this approach often leads to an increase in the band gap, which can adversely affect electrical performance and limit the enhancement of device sensitivity.[22] Therefore, it is crucial to develop a new strategy that enables precise modulation of the band gap and enhances electrical performance without compromising structural stability.[14]

In this regard, the concept of "lone-pair cations" offers a novel design strategy.[23–25] In molecular frontier orbitals, non-bonding lone-pair electrons typically occupy the top of the highest occupied molecular orbital (HOMO) gap, which can significantly influence electronic states near the valence band maximum (VBM).[14] By introducing lone-pair electrons near the band edges, it is possible to achieve band gap contraction and optimize the band-edge, thereby enhancing the intrinsic electrical conductivity and carrier mobility of the material, and improving the electrical properties of the material.[24] More importantly, lone-pair electrons are stereochemically active and repel surrounding anions, which lead to the distortion of the coordination octahedra.[26] Significant distortion might further induce the structural reconstruction toward lower-dimensional structures, such as one-dimensional (1D) perovskites.[27]

Low-dimensional perovskites, especially 1D perovskites, demonstrate notable advantages due to their unique crystal structures, including carrier transport in directional selectivity, suppressed non-radiative recombination, and enhanced structural stability.[28–31] In 1D MFPs, co-planar octahedra form chain-like frameworks separated by large organic cations. This 1D structure provides two key advantages. Firstly, the organic cations create physical barriers that suppress ion migrations, improving both the environmental and operational stability of the perovskites.[29] Secondly, the 1D structure provides anisotropic charge transport channels, allowing efficient electron transport along specific directions, which is essential for improving the performance of X-ray detectors.[31] Simultaneously, the organic components act as natural passivators, substantially reducing defect state density and thereby suppressing non-radiative recombination, ultimately leading to excellent electrical performance in specific directions.[32] Building upon these advantages, we propose a strategy that utilizes lone-pair cations to regulate dimensionality and optimize band-edge, with the goal of designing MFPs that combine high structural stability and efficient charge transport performance in specific directions (Fig. 1).

In this work, we focus on the synthesis and characterization of a new 1D MFP, DABCO-$N_2H_5(BF_4)_3$, in which the $N_2H_5^+$ cation with a lone pair of electrons and a relatively large ionic radius is introduced into the DABCO-$NH_4(BF_4)_3$ [22,33] (DABCO = 1,4-diazabicyclo[2.2.2]octane) template, which is proposed as a stable structural template for MFPs with high structural stability and low noise current. Initially, DABCO-$NH_4(BF_4)_3$ adopts a three-dimensional (3D) crystal structure, but through the introduction of $N_2H_5^+$, the structure distorts in the coordination octahedra due to steric repulsion from the lone-pair electrons

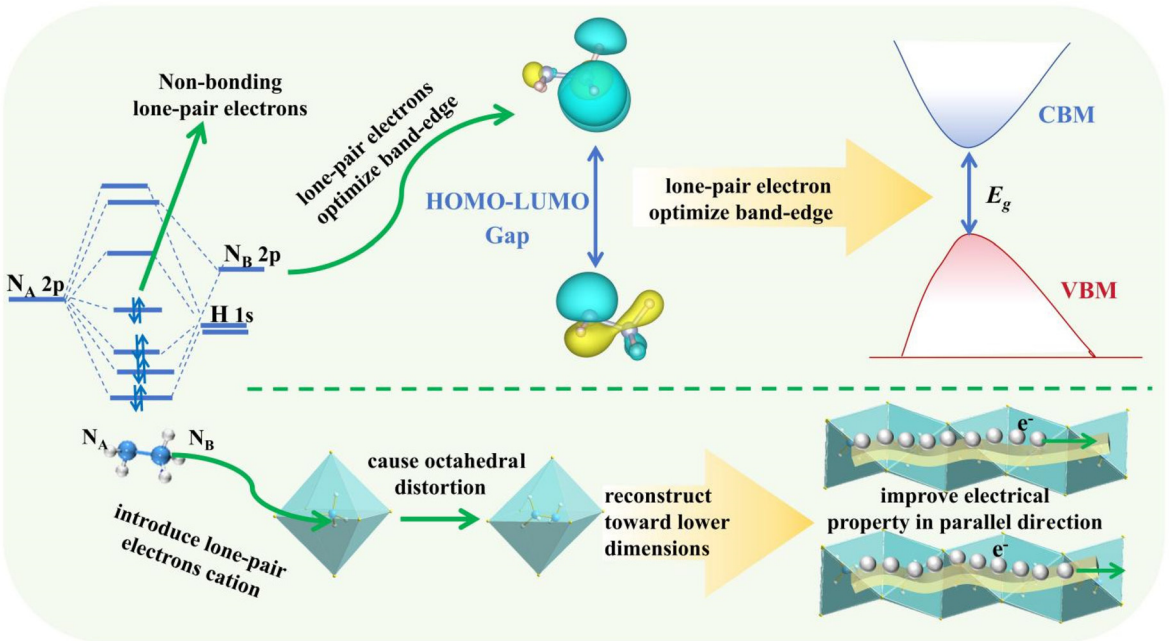

Fig. 1 Schematic illustration of a lone-pair cation driving dimensionality regulation and optimizing the band-edge strategy for improving the X-ray detection properties of MFPs.

and undergoes a transformation to a 1D structure, which effectively reduces the material's dimensionality. This transformation enhances anisotropic charge transport and optimizes the band-edge, improving electrical conductivity and carrier mobility. The 1D structure also improves structural stability, suppressing ion migrations. These results from our experiments demonstrate that the DABCO-$N_2H_5(BF_4)_3$ not only enhances structural stability but also significantly improves carrier transport and X-ray detection performance. The 1D MFP structure, combined with $N_2H_5^+$, optimizes charge transport along the parallel direction, achieving an ultrahigh sensitivity of 2570 μC Gy_{air}^{-1} cm^{-2} at 50 V, and a low detection limit of 20.9 nGy_{air} s^{-1}. These results indicate that DABCO-$N_2H_5(BF_4)_3$ is a promising material for high-performance X-ray detection, offering enhanced sensitivity, low detection limits, and high stability under various operating conditions.

Results and discussion

The template compound DABCO-$NH_4(BF_4)_3$ crystallizes in the cubic space group $Pa\bar{3}$ (Fig. 2a), exhibiting a 3D structure. In this structure, six BF_4^- anions coordinate with one NH_4^+ cation to form an octahedron, with the NH_4^+ cation located at the centre (Fig. 2b). Upon introducing the $N_2H_5^+$ cation, characterized by its lone-pair electrons and a relatively large ionic radius, into the B-site, significant distortion of the octahedron occurs (Fig. 2c). The $N_2H_5^+$ cation occupies the centre of the distorted octahedron. These distorted $[(N_2H_5)(BF_4)_6]$ octahedra are linked co-planarly along the *b*-axis, creating a 1D chain structure. The A-site $DABCO^{2+}$ cations are anchored to these chains through N–H···F hydrogen bonding interactions, resulting in the formation of a new 1D MFP crystal, DABCO-$N_2H_5(BF_4)_3$ (Fig. 2d). The degrees of distortion of both $[NH_4(BF_4)_6]$ and $[N_2H_5(BF_4)_6]$ octahedra are calculated (Fig. S1), revealing that the distortion in the $[N_2H_5(BF_4)_6]$ octahedron is significantly greater than that in the $[NH_4(BF_4)_6]$ octahedron. This indicates that the introduction of the $N_2H_5^+$ cation, with one lone-pair of electrons and a larger ionic radius, plays a critical role in altering the crystal structure and facilitating the transition to a 1D crystal arrangement. Furthermore, the Goldschmidt tolerance factors (t) for DABCO-$NH_4(BF_4)_3$ and DABCO-$N_2H_5(BF_4)_3$ are calculated to be 0.88 and 0.75, respectively (Tables S1 and S2), which might be responsible for the structural change from a co-vertex octahedral linkage in DABCO-$NH_4(BF_4)_3$ to a co-planar octahedral linkage in DABCO-$N_2H_5(BF_4)_3$.

DABCO-$N_2H_5(BF_4)_3$ crystallizes in the monoclinic space group $P2_1/m$. The detailed crystallographic data and structure refinement information of DABCO-$NH_4(BF_4)_3$ and DABCO-$N_2H_5(BF_4)_3$ are summarized in Tables S3–S9. High-quality single crystals of DABCO-$NH_4(BF_4)_3$ and DABCO-$N_2H_5(BF_4)_3$ were obtained *via* the solution evaporation method, with approximate dimensions of 5 × 5 × 1.5 mm^3 and 6 × 4 × 2 mm^3, respectively (Fig. 2g and h). The natural growth surfaces of single crystal DABCO-$NH_4(BF_4)_3$ and single DABCO-$N_2H_5(BF_4)_3$ are (002) and (−405), respectively (Fig. 2e, f and Fig. S2, S3). Rocking curve measurements were carried out and the results are shown in Fig. S4 and S5. The full width at half maximum (FWHM) values of DABCO-$NH_4(BF_4)_3$ and DABCO-$N_2H_5(BF_4)_3$ are 0.0231° and 0.0111°, respectively, indicating high crystallinity and quality of DABCO-$NH_4(BF_4)_3$ and DABCO-$N_2H_5(BF_4)_3$ single crystals. Furthermore, EDS mapping results confirm the homogeneity and high quality of both single-crystal samples (Fig. S6 and S7).

In order to further explore the structural stabilities of the MFPs DABCO-$NH_4(BF_4)_3$ and DABCO-$N_2H_5(BF_4)_3$ crystals, we investigated their thermodynamic properties, the hydrogen bonding strength in structures, the energy required for defect formation, as well as the energies associated with ion migrations. The thermodynamic properties of DABCO-$NH_4(BF_4)_3$ and DABCO-$N_2H_5(BF_4)_3$ crystals are explored and shown in Fig. S8 and S9. Thermogravimetric analysis (TGA) shows that their thermal decomposition temperatures are 250 °C and 255 °C, respectively, demonstrating their high thermal stability.

The strength of hydrogen bonds in the structures of DABCO-$NH_4(BF_4)_3$ and DABCO-$N_2H_5(BF_4)_3$ is investigated using the independent gradient model based on Hirshfeld partition (IGMH). The IGMH analysis visually distinguishes the nature and strength of intermolecular interactions: blue regions indicate attractive and stabilizing forces, red regions represent repulsive and destabilizing forces, and green regions correspond to van der Waals interactions. As shown in Fig. 2i and j, strong hydrogen bonding interactions are observed between $DABCO^{2+}$ and BF_4^-, as well as between NH_4^+ and BF_4^- in DABCO-$NH_4(BF_4)_3$. Similarly, in DABCO-$N_2H_5(BF_4)_3$, pronounced hydrogen bonding interactions exist between $DABCO^{2+}$ and BF_4^-, and between $N_2H_5^+$ and BF_4^-. These strong hydrogen bonds contribute to enhanced lattice rigidity and effectively suppress ion migrations.[18] Furthermore, a comparative analysis of hydrogen bond lengths reveals that the average N–H(NH_4)···F distance in DABCO-$NH_4(BF_4)_3$ is 3.015 Å, whereas in DABCO-$N_2H_5(BF_4)_3$ the average N–H(N_2H_5)···F distance is shortened to about 2.972 Å (Fig. S10). To further quantify the influence of $N_2H_5^+$ substitution, we conducted 2D Hirshfeld surface analysis to visualize the intermolecular interactions. As shown in Fig. S23, the dominant H···F hydrogen bonds account for 66.1% of all contacts in DABCO-$NH_4(BF_4)_3$. After substituting NH_4^+ with $N_2H_5^+$, this proportion increases to 71.8%. These findings collectively demonstrate that the introduction of the $N_2H_5^+$ group could strengthen the hydrogen bonding network in the MFPs, thereby improving the structural stability and rigidity.[27]

To further investigate the structural stabilities of DABCO-$NH_4(BF_4)_3$ and DABCO-$N_2H_5(BF_4)_3$, we studied the energies required for the formation of vacancy defects and the energies required for ion migration in DABCO-$NH_4(BF_4)_3$ and DABCO-$N_2H_5(BF_4)_3$. Based on density functional theory (DFT) calculations, we separately simulated the defect formation energies of H ions at the A-site and B-site and those of F ions at the X-site in DABCO-$NH_4(BF_4)_3$ and DABCO-$N_2H_5(BF_4)_3$ crystals. As shown in Fig. S11, in DABCO-$NH_4(BF_4)_3$, the formation energies of H(+1) in $DABCO^{2+}$ and H(−1) in $DABCO^{2+}$ are relatively low, indicating that H ions at the A-site are the most prone to migration. In DABCO-$N_2H_5(BF_4)_3$, low defect for-

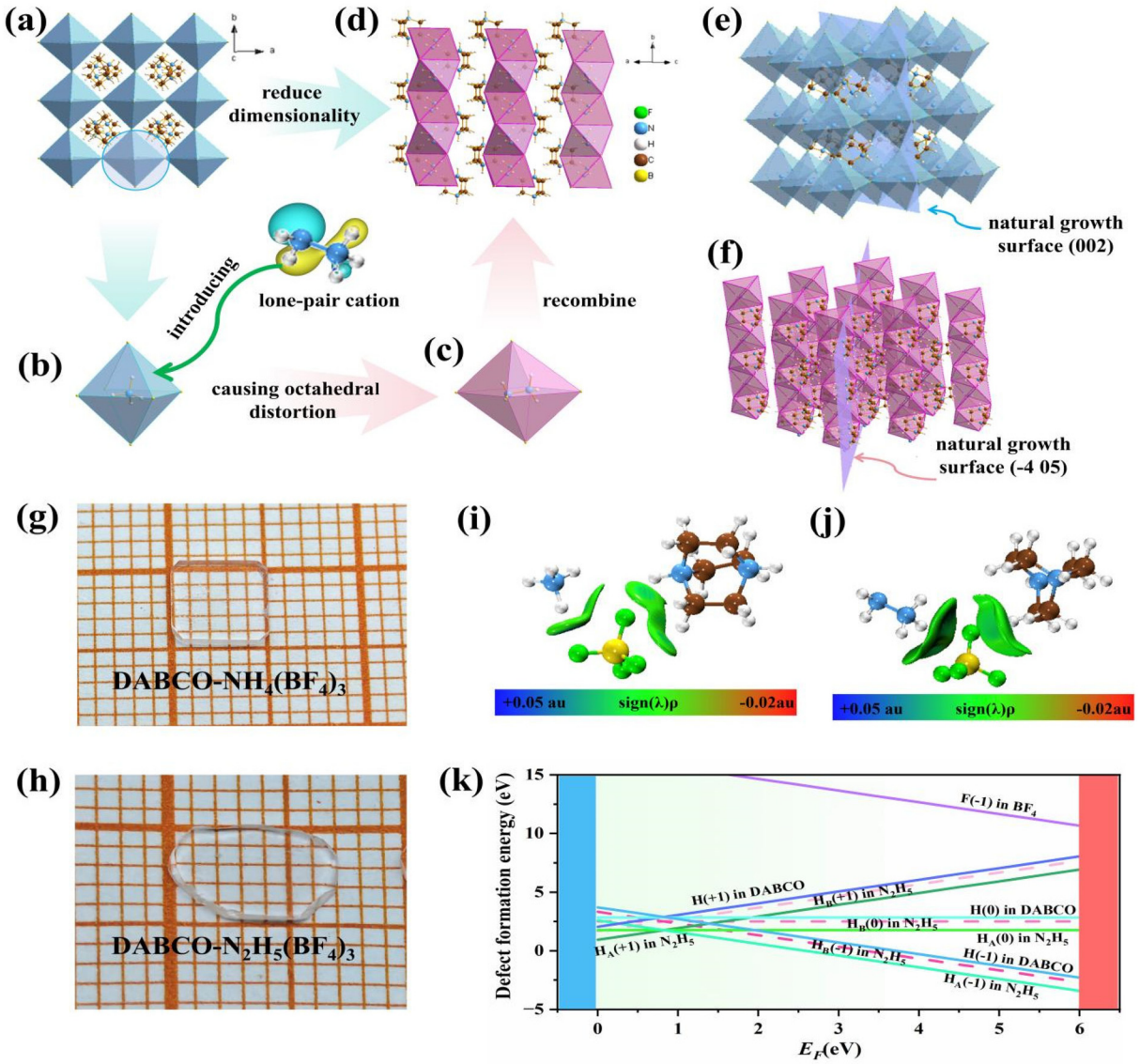

Fig. 2 (a) Crystal structure of DABCO-$NH_4(BF_4)_3$. (b) The NH_4X_6 octahedron. (c) The $N_2H_5X_6$ octahedron. (d) Crystal structure of DABCO-$N_2H_5(BF_4)_3$. (e) Natural growth morphology of DABCO-$NH_4(BF_4)_3$ crystals, exposing the (002) surface. (f) Natural growth morphology of DABCO-$N_2H_5(BF_4)_3$ crystals, exposing the (−405) surface. (g) The image of DABCO-$NH_4(BF_4)_3$. (h) The image of a DABCO-$N_2H_5(BF_4)_3$ single crystal. (i) Isosurface map of DABCO-$NH_4(BF_4)_3$. (j) Isosurface map of DABCO-$N_2H_5(BF_4)_3$. (k) Defect formation energy of DABCO-$N_2H_5(BF_4)_3$ with different components.

mation energies are observed for $H_A(+1)$ in N_2H_5 and $H_A(-1)$ in N_2H_5 (Fig. 2k). Here, H_A represents the H atom attached to the N_A atom bearing a lone pair of electrons in the N_2H_5, while H_B refers to the H atom on the N_B without a lone pair of electrons in N_2H_5. This suggests that in DABCO-$N_2H_5(BF_4)_3$, the H ion on the N_A atom with one lone pair of electrons in $N_2H_5^+$ is the most prone to migration. In the structures of both DABCO-$NH_4(BF_4)_3$ and DABCO-$N_2H_5(BF_4)_3$, the formation energies for F vacancies are relatively high, which is attributed to the strong hydrogen bond interactions between F and H. It is worth noting that defects located near the valence band may lead to ion migrations, thereby affecting the magnitude of the dark current. Conversely, defects located near the conduction band minimum (CBM) could form shallow defect levels, which helps regulate the number of electrons near the conduction band and optimizes the electrical properties. Therefore, we designed ion migration paths for DABCO-$NH_4(BF_4)_3$ and DABCO-$N_2H_5(BF_4)_3$ based on their lowest defect formation energies (Fig. S12) and calculated the corresponding ion migration barriers, separately. Both DABCO-$NH_4(BF_4)_3$ and DABCO-$N_2H_5(BF_4)_3$ have relatively high ion migration barriers (Fig. S13 and Table S12), which contributes to the structural stability of the MFPs and reduction of noise current.[34]

Ion migrations in MFPs can severely compromise the stability and performance of optoelectronic devices. Significant ion migration might lead to an increase in noise current in X-ray

detectors, resulting in substantial dark current drift and higher detection limits.[17] Based on this, we conducted experiments to study the ion migration within the DABCO-$NH_4(BF_4)_3$ and DABCO-$N_2H_5(BF_4)_3$ single crystal (SC) devices. In MFPs, ion migration typically causes pronounced hysteresis between forward and reverse current–voltage (*I–V*) sweep curves, manifesting as current lagging or tailing. Thus, the extent of ion migration can be preliminarily assessed by comparing the discrepancies between the forward and reverse *I–V* sweeps. As shown in Fig. S14, for the entire scanning process of the DABCO-$NH_4(BF_4)_3$ and DABCO-$N_2H_5(BF_4)_3$ SC detectors, the forward and reverse *I–V* scanning curves nearly overlap, indicating that there is negligible ion migration in these two MFPs. Furthermore, current–time (*I–T*) measurements of the DABCO-$NH_4(BF_4)_3$ and DABCO-$N_2H_5(BF_4)_3$ SC devices under a wide range of dose rates and different bias voltages show a stable increase in current with almost no delay or tailing (Fig. S15). This also proves the excellent operational stability of DABCO-$NH_4(BF_4)_3$ and DABCO-$N_2H_5(BF_4)_3$ SC devices.

The high sensitivity of the MFP detector is closely associated with its superior electrical properties, which in turn are strongly dependent on the band gap and band structure.[35,45] To further investigate how lone-pair cations optimize the band structure, we performed DFT calculations to analyze the band structures and orbital contributions of DABCO-$NH_4(BF_4)_3$ and DABCO-$N_2H_5(BF_4)_3$. As shown in Fig. 3a, DABCO-$NH_4(BF_4)_3$ exhibits a large band gap of 8.13 eV. Based on the partial density of states (PDOS) (Fig. S16a) and band contribution diagrams (Fig. S17a), the CBM is primarily contributed by the $DABCO^{2+}$ cations, whereas the VBM mainly originates from the BF_4^- anions. DABCO-$N_2H_5(BF_4)_3$ has a significantly narrower band gap of 5.48 eV (Fig. 3b). The band contribution analysis reveals that in DABCO-$N_2H_5(BF_4)_3$, the VBM is dominated by the $N_2H_5^+$ group, while the CBM arises from the $DABCO^{2+}$ cation (Fig. S17b). The PDOS diagram also shows that the lone-pair-cation $N_2H_5^+$ contributes to the VBM (Fig. S16b). These results confirm that lone-pair-cation $N_2H_5^+$ could effectively reduce the band gap and optimize the band structure, thereby enhancing electrical performance. To further clarify the role of the lone-pair-cation $N_2H_5^+$, we conducted a further analysis of the contributions of the two different N atoms on the $N_2H_5^+$ group. As shown in Fig. 3c, in $N_2H_5^+$ the N_A atom carries one lone pair of electrons, while the N_B atom does not. The VBM is almost entirely contributed by N_A atoms. This confirms that the lone-pair electrons in $N_2H_5^+$ cations directly influence the band gap magnitude, playing a critical role in band structure optimization and the improvement of electrical properties.[24]

The naturally grown surfaces of DABCO-$NH_4(BF_4)_3$ and DABCO-$N_2H_5(BF_4)_3$ are identified as the (002) and (−405) planes, respectively (Fig. S2 and S3). Since DABCO-$NH_4(BF_4)_3$ crystallizes in the cubic system and exhibits isotropic properties, the electrode contact is fabricated directly on its (002) surface (Fig. 3d). However, DABCO-$N_2H_5(BF_4)_3$ crystallizes in the monoclinic system and has a 1D perovskite structure, with pronounced anisotropy.[36] Its natural growth surface (−405) passes through the octahedral chains within the DABCO-$N_2H_5(BF_4)_3$ crystal structure (Fig. 2f), and the crystal morphology is clearly elongated. Therefore, electrodes are deposited along two distinct orientations. One electrode is deposited parallel to the 1D chain within the long side direction of the (−405) plane of the DABCO-$N_2H_5(BF_4)_3$ crystal, the other electrode is deposited perpendicular to the 1D chain direction in the direction perpendicular to the (−405) plane (Fig. 3e).

The X-ray attenuation capabilities of DABCO-$NH_4(BF_4)_3$ and DABCO-$N_2H_5(BF_4)_3$ are investigated across a broad energy spectrum. Their absorption coefficients are calculated within the energy range from 0.001 to 100 MeV, and the X-ray absorption performance is evaluated using the relationship $\alpha \propto \rho Z^4/E^3$. As shown in Fig. S18, the DABCO-$NH_4(BF_4)_3$ and DABCO-$N_2H_5(BF_4)_3$ exhibit very similar absorption coefficients and comparable X-ray attenuation abilities, which is primarily attributed to their identical elemental composition.

To further elucidate the carrier behavior of the DABCO-$NH_4(BF_4)_3$ and DABCO-$N_2H_5(BF_4)_3$ SC devices, especially along different crystallographic directions in the DABCO-$N_2H_5(BF_4)_3$ SC device, we measured the photocurrent and the critical $\mu\tau$ (mobility–lifetime) product of these two SC detectors. The electrical performances of DABCO-$NH_4(BF_4)_3$ and DABCO-$N_2H_5(BF_4)_3$ SC detectors under X-ray irradiation are evaluated by comparing the photocurrents under identical exposure conditions. As shown in Fig. 3f, the DABCO-$NH_4(BF_4)_3$ SC detector exhibits 60% smaller current density than that of the DABCO-$N_2H_5(BF_4)_3$ SC detector measured along the parallel direction. Moreover, the current density along the parallel direction of the DABCO-$N_2H_5(BF_4)_3$ SC detector is approximately 160% greater than that of DABCO-$N_2H_5(BF_4)_3$ in the perpendicular direction. These experimental results collectively demonstrate that the lone-pair cation not only enhances the overall electrical performance compared to DABCO-$NH_4(BF_4)_3$, but also leads to superior charge transport along the direction of the 1D chain in the DABCO-$N_2H_5(BF_4)_3$ SC detector. To obtain the $\mu\tau$ products of DABCO-$NH_4(BF_4)_3$ and DABCO-$N_2H_5(BF_4)_3$ SC detectors, the photoconductivity curves of the SC detectors were measured under a fixed X-ray dose. A modified Hecht equation was then used to fit these curves, based on the corresponding *I–V* characteristics. As presented in Fig. 3g, the $\mu\tau$ value for the DABCO-$NH_4(BF_4)_3$ SC detector is 1.01×10^{-4} cm^2 V^{-1}, while the $\mu\tau$ value for the DABCO-$N_2H_5(BF_4)_3$ SC detector reaches 1.47×10^{-4} cm^2 V^{-1} along the parallel direction, and 5.87×10^{-5} cm^2 V^{-1} along the perpendicular direction. These data further confirm that introducing the lone-pair cation effectively improves carrier transport and charge extraction, thereby enhancing the overall electrical performance of the MFPs.

Sensitivity is a critical performance parameter for X-ray detection materials as high sensitivity enables more efficient conversion of X-ray energy into electrical signals, thereby realizing high-performance detection. The DABCO-$NH_4(BF_4)_3$ and DABCO-$N_2H_5(BF_4)_3$ SC devices are systematically evaluated under various bias voltages and different X-ray dose rates. As shown in Fig. 3h and i, the photocurrent increases markedly

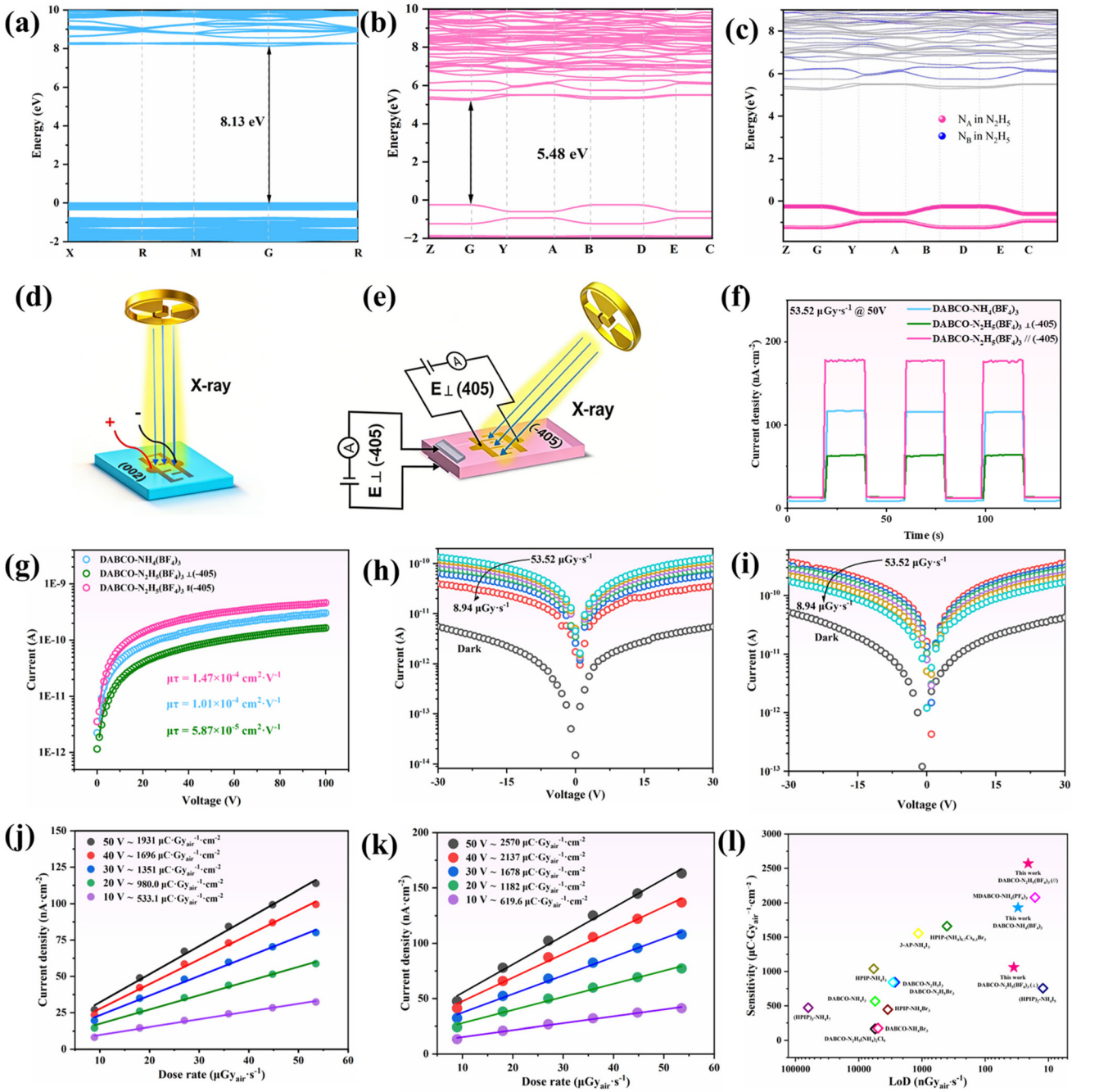

Fig. 3 The calculated band structures of (a) DABCO-$NH_4(BF_4)_3$ and (b) DABCO-$N_2H_5(BF_4)_3$. (c) The influence of lone-pair cation $N_2H_5^+$ on the band structure. (d) Schematic illustration of the devices based on DABCO-$NH_4(BF_4)_3$ and (e) DABCO-$N_2H_5(BF_4)_3$. (f) The measured current density comparison between DABCO-$NH_4(BF_4)_3$ and DABCO-$N_2H_5(BF_4)_3$ with both parallel and perpendicular directions. (g) The comparison of $\mu\tau$ products between DABCO-$NH_4(BF_4)_3$ and DABCO-$N_2H_5(BF_4)_3$ with both parallel and perpendicular directions. (h) The irradiated *I–V* curves of the DABCO-$NH_4(BF_4)_3$ SC device and (i) DABCO-$N_2H_5(BF_4)_3$ SC device along the parallel direction under different dose rates. (j) X-ray responses of current density with various dose rates at different bias voltages for the DABCO-$NH_4(BF_4)_3$ SC device and (k) DABCO-$N_2H_5(BF_4)_3$ SC device along the parallel direction. (l) The sensitivity and limit of detection (LoD) comparisons of the reported MFPs under a bias voltage of 50 V.

as the dose rate rises from 8.94 to 53.52 $\mu Gy_{air}\ s^{-1}$, demonstrating the excellent radiation response characteristics of these two SC detectors. The sensitivity is extracted by linearly fitting the photocurrent density under X-ray irradiation against the applied dose rate at each bias voltage. As presented in Fig. 3j and k, the DABCO-$NH_4(BF_4)_3$ SC device achieves a sensitivity of 1931 $\mu C\ Gy_{air}^{-1}\ cm^{-2}$ at 50 V. The sensitivities of the DABCO-$N_2H_5(BF_4)_3$ SC device reach 2570 $\mu C\ Gy_{air}^{-1}\ cm^{-2}$ along the parallel direction and 1061 $\mu C\ Gy_{air}^{-1}\ cm^{-2}$ along the perpendicular direction (Fig. S19), exhibiting great an-

isotropy. These results indicate that the introduction of the lone-pair cation effectively optimizes the electrical properties of 1D DABCO-$N_2H_5(BF_4)_3$ in the chain direction, enabling superior sensitivity along its 1D chain direction. Notably, these sensitivities substantially exceed those of most reported MFPs (Fig. 3l).

The resistivity of DABCO-$NH_4(BF_4)_3$ and DABCO-$N_2H_5(BF_4)_3$ is measured under both X-ray on and off conditions (Fig. S20). In the dark, the resistivity of DABCO-$NH_4(BF_4)_3$ was determined to be 8.46×10^{11} Ω cm, while the resistivities of DABCO-$N_2H_5(BF_4)_3$ are determined to be 6.26×10^{10} Ω cm along the parallel direction and 1.03×10^{11} Ω cm along the perpendicular direction, respectively. These values are significantly higher than those of most reported MFPs (Table S10), which can be attributed to the wide band gaps of both MFPs. A large resistivity effectively suppresses thermally excited carriers, thereby significantly reducing dark current noise.[37] Furthermore, the dark current drift (D) serves as a critical parameter that directly reflects the stability of the dark current during device operation. As shown in Fig. 4a, under a constant electric field of 10 V mm^{-1}, long-term baseline test of the DABCO-$NH_4(BF_4)_3$ SC devices yields very low dark current drift values of 3.79×10^{-7} nA cm^{-1} s^{-1} V^{-1}, while the DABCO-$N_2H_5(BF_4)_3$ SC detector exhibits extremely low current values of 3.37×10^{-7} nA cm^{-1} s^{-1} V^{-1} along the parallel direction and 2.58×10^{-7} nA cm^{-1} s^{-1} V^{-1} along the perpendicular direction, respectively. Even under the electric fields of 666.6 V mm^{-1} and 1333.3 V mm^{-1}, the dark current drifts of DABCO-$N_2H_5(BF_4)_3$ crystals are 3.88×10^{-7} nA V^{-1} cm^{-1} s^{-1} and 5.97×10^{-7} nA V^{-1} cm^{-1} s^{-1}, respectively, remaining at a very low level (Fig. S24). Such ultralow dark current drifts enable the DABCO-$NH_4(BF_4)_3$ and DABCO-$N_2H_5(BF_4)_3$ SC devices to maintain stable performance under varying environmental conditions. These observations confirm that DABCO-$NH_4(BF_4)_3$ and DABCO-$N_2H_5(BF_4)_3$ SC detectors possess very low noise currents, which is advantageous for lowering the detection limit in MFP-based X-ray detectors.

The detection limit represents a critical performance metric for X-ray detectors. The lower the detection limit is, the more subtle changes the detector can distinguish, reflecting a high signal-to-noise ratio (SNR). Therefore, low detection limits will greatly expand the application prospects of the devices. We record the SNR of the SC detectors at various bias voltages. As displayed in Fig. 4b–d, the DABCO-$NH_4(BF_4)_3$ SC detector achieves a detection limit of 30.2 nGy_{air} s^{-1} at SNR = 3. While the DABCO-$N_2H_5(BF_4)_3$ SC device reaches 20.9 nGy_{air} s^{-1} along the parallel direction and 35.3 nGy_{air} s^{-1} along the perpendicular direction. These values are considerably lower than those of most reported metal-containing[38–43] and MFP X-ray detectors (Table S11), and are approximately 200 times lower than the standard requirement for medical diagnostics (~5500 nGy_{air} s^{-1}). Such outstanding performance can be attributed to the ultrahigh resistivity and the stable low dark current of both MPFs, which together effectively suppress noise current and

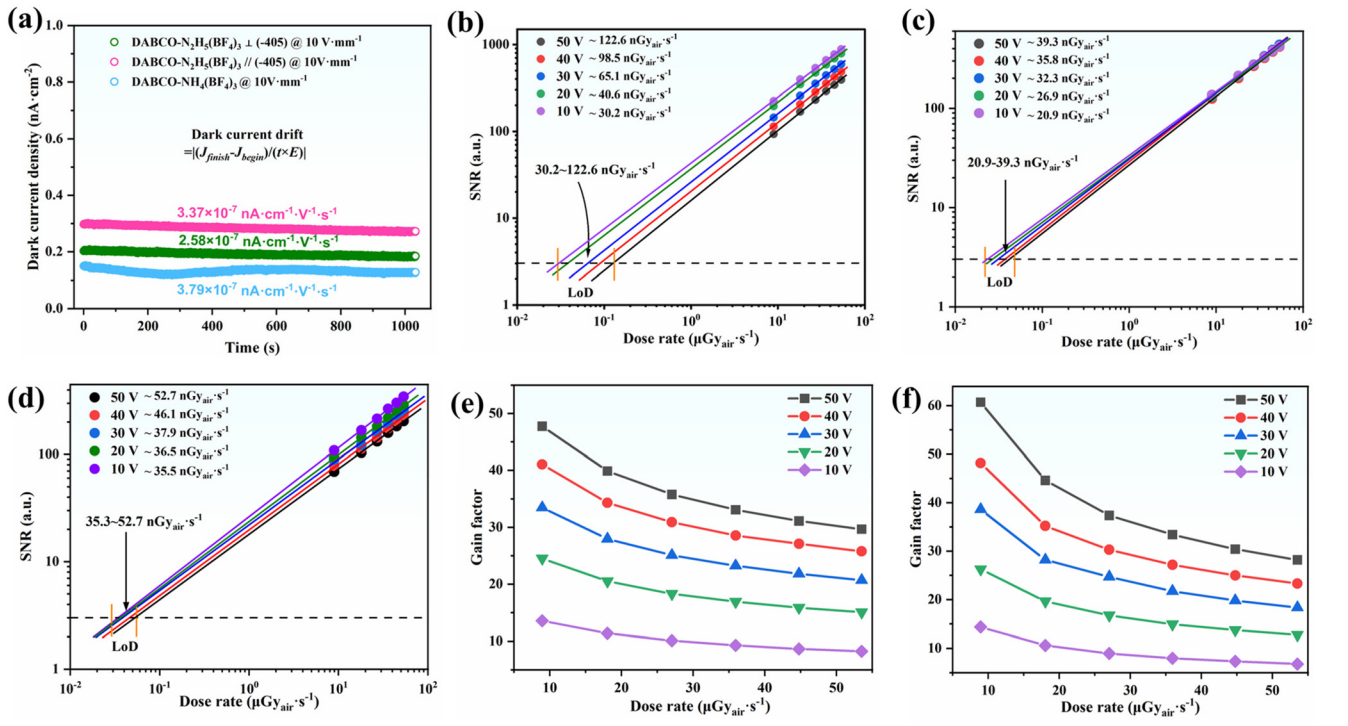

Fig. 4 (a) Dark current drift of DABCO-$NH_4(BF_4)_3$ and DABCO-$N_2H_5(BF_4)_3$ with both parallel and perpendicular directions under an electric field of 10 V mm^{-1}. (b) The signal-to-noise ratio for detection-limits at different bias voltages of the DABCO-$NH_4(BF_4)_3$ SC device, (c) DABCO-$N_2H_5(BF_4)_3$ SC device along the parallel and (d) perpendicular directions. (e) The gain factors of DABCO-$NH_4(BF_4)_3$ and (f) DABCO-$N_2H_5(BF_4)_3$.

highlight their strong potential for detecting weak X-ray irradiation.

Owing to their robust structural stabilities, the DABCO-$NH_4(BF_4)_3$ and DABCO-$N_2H_5(BF_4)_3$ SC detectors exhibit stable operation abilities even under ultrahigh bias voltages. As shown in Fig. S21 and S22, when under the bias voltage of 100 V, DABCO-$NH_4(BF_4)_3$ achieves a sensitivity of 3016 μC Gy_{air}^{-1} cm^{-2} and a detection limit of 164 nGy_{air} s^{-1}. In comparison, the DABCO-$N_2H_5(BF_4)_3$ SC detector exhibits a sensitivity of 3509 μC Gy_{air}^{-1} cm^{-2} and a detection limit of 131 nGy_{air} s^{-1} along the parallel direction, while along the perpendicular direction, the sensitivity is 1569 μC Gy_{air}^{-1} cm^{-2} and the detection limit is 120 nGy_{air} s^{-1}, respectively. At 200 V, DABCO-$NH_4(BF_4)_3$ shows a sensitivity of 4506 μC Gy_{air}^{-1} cm^{-2} and a detection limit of 272 nGy_{air} s^{-1}. Under the same bias voltage, the DABCO-$N_2H_5(BF_4)_3$ SC detector reaches a sensitivity of 5041 μC Gy_{air}^{-1} cm^{-2} and detection limits of 267 nGy_{air} s^{-1} along the parallel direction and 2180 μC Gy_{air}^{-1} cm^{-2} with 221 nGy_{air} s^{-1} along the perpendicular direction. These results demonstrate that the DABCO-$N_2H_5(BF_4)_3$ SC detector could maintain robust stability and better detection performance than the DABCO-$NH_4(BF_4)_3$ SC detector across a wide range of operating conditions, highlighting its promising potential for practical applications.

The gain factor is a key parameter that characterizes the ability of a detector to amplify the converted electrical signal after receiving incident radiation, which significantly influences the overall detector performance.[44] As shown in Fig. 4e and f, at a fixed bias voltage, the gain factors of both DABCO-$NH_4(BF_4)_3$ and DABCO-$N_2H_5(BF_4)_3$ SC detectors decrease with increasing X-ray dose rates. Conversely, under a constant dose rate, the gain factors increase with a higher applied bias voltage. This behavior is consistent with the gain compression effect observed during dynamic range enhancement. Consequently, the DABCO-$NH_4(BF_4)_3$ and DABCO-$N_2H_5(BF_4)_3$ SC detectors are more suitable for operation under high bias voltages and low dose rates, which enables higher X-ray response sensitivities.

The environmental stability and long-term operational stability of X-ray detectors are crucial for their practical applications.[18] Therefore, we systematically evaluate the stability of the DABCO-$N_2H_5(BF_4)_3$ SC detector. The DABCO-$N_2H_5(BF_4)_3$ SC detector is exposed to ambient conditions, such as 24 °C temperature and 31% relative humidity, and characterized by XRD after 30 and 60 days (Fig. 5a). The experiments show that the diffraction patterns remain highly consistent with the initial one, indicating no decomposition or phase transformation. The stabilities, sensitivities and dark currents under different temperature conditions were tested and are shown in Fig. S26, which proved the excellent operation stability of DABCO-$N_2H_5(BF_4)_3$ even at elevated temperatures. These results prove that the DABCO-$N_2H_5(BF_4)_3$ SC device exhibits excellent environmental stability. More importantly, the photocurrent and sensitivity of the DABCO-$N_2H_5(BF_4)_3$ SC device under different X-ray dose rates are measured at the first, 30th and 60th days.

Compared with the initial values, the photocurrent decreases by only about 0.5% after 30 days and 1.1% after 60 days (Fig. 5b), while the sensitivities show a very minor reduction, approximately 1% to 2.7% (Fig. 5d) for the DABCO-$N_2H_5(BF_4)_3$ SC detector. This slight degradation in sensitivity may be attributed to mild diffusion of the silver electro-

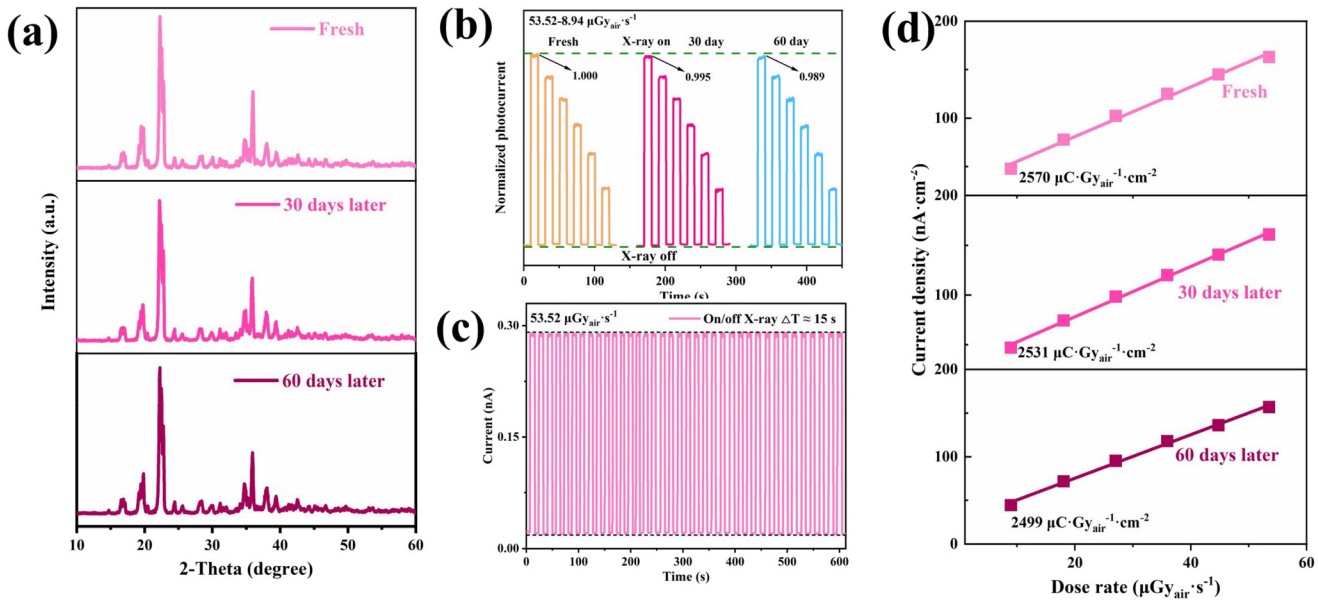

Fig. 5 (a) PXRD patterns of DABCO-$N_2H_5(BF_4)_3$ during the fresh state and after 30 and 60 days of exposure to the air. (b) Comparison of the photocurrent of DABCO-$N_2H_5(BF_4)_3$ SC in the fresh state and when exposed to air for 30 and 60 days under different X-ray doses with a bias voltage of 50 V. (c) Long-term on/off cycling stability of the DABCO-$N_2H_5(BF_4)_3$ SC device at a 50 V bias voltage for 600 s. (d) Sensitivities of the DABCO-$N_2H_5(BF_4)_3$ SC device when fresh and when exposed to air for 30 and 60 days.

des, confirming that the devices can maintain stable performance under natural ambient conditions.[18] To further examine the stability under continuous operation, we perform a repeated X-ray on/off cycling test. During multiple switching cycles with a period of 15 s over a total duration of 600 s, the current response of the devices exhibited excellent repeatability without noticeable decay (Fig. 5c). In addition, the irradiation stability of DABCO-$N_2H_5(BF_4)_3$ was evaluated under prolonged X-ray irradiation. As shown in Fig. S25, the device was continuously irradiated for 600 s at a fixed dose rate of 1.989 mGy s^{-1}, with bias voltages of 100 V and 200 V, respectively. Over the entire testing period, the photocurrent showed no obvious degradation or fluctuation. The total dose of X-rays absorbed by the DABCO-$N_2H_5(BF_4)_3$ SC detector reached 2.22 Gy. These findings prove that the DABCO-$N_2H_5(BF_4)_3$ SC detector exhibits outstanding environmental and operational stability, highlighting its strong potential as a promising direct X-ray detection material.

Conclusions

In conclusion, we present a novel approach to the design of high-performance MFPs by utilizing the lone-pair cation strategy to regulate dimensionality and optimize the band-edge. By introducing the $N_2H_5^+$ cation with a lone pair of electrons and a relatively large ionic radius, we successfully achieved the transformation of a 3D perovskite to a 1D perovskite, which results in enhanced structural stability and improved electrical performance. Both theoretical calculations and experimental results demonstrate that, benefiting from its 1D chain structure and strong hydrogen bond interactions, the DABCO-$N_2H_5(BF_4)_3$ SC device exhibits extremely low dark-current drift and effectively suppresses ion migration within the crystal. The 1D structure promotes anisotropic charge transport along the parallel direction, optimizes the band edge, and leads to superior carrier mobility and enhanced electrical performance. Owing to these advantages, the DABCO-$N_2H_5(BF_4)_3$ SC device exhibits outstanding detection performance along the parallel direction, achieving an ultra-high sensitivity of 2570 μC Gy_{air}^{-1} cm^{-2} at 50 V, and a low detection limit of 20.9 nGy_{air} s^{-1}. The excellent stability of the DABCO-$N_2H_5(BF_4)_3$ SC device enables it to operate stably under a bias of 200 V, while achieving a sensitivity of 5041 μC Gy_{air}^{-1} cm^{-2} and a detection limit as low as 267 nGy_{air} s^{-1}. Furthermore, environmental stability tests confirm that the DABCO-$N_2H_5(BF_4)_3$ SC device maintains long-term stable performance even under harsh conditions. These results indicate that DABCO-$N_2H_5(BF_4)_3$ is a promising material for high-performance X-ray detection, offering enhanced sensitivity, low detection limits, and high stability under various operating conditions. This work presents a novel approach to effectively balance and optimize both structural stability and electrical properties, providing a new path for developing high-performance, low-dose, and highly stable X-ray detection materials.

Author contributions

Min Luo and Huixin Fan provided research ideas, supervised the entire study, and revised the manuscript. Jiasheng Gong wrote the initial draft and carried out the experiments and measurements. Chensheng Lin contributed to the theoretical calculations. Pengxiang Dong contributed to the analysis of the performances. Chunlei Yu and Tao Yan contributed to the experiments on optoelectronic properties. The manuscript was written through the contributions of all authors.

Conflicts of interest

The authors declare no conflict of interest.

Data availability

The data supporting this study's findings are available in this article's supplementary information (SI). Supplementary information is available. The additional optical, electronic properties have been shown in the Supplementary Information. See DOI: **https://doi.org/10.1039/d6qi00393a**.

CCDC 2528731 (DABCO-$N_2H_5(BF_4)_3$) contains the supplementary crystallographic data for this paper.[47]

Acknowledgements

This work was supported by the Natural Science Foundation of Fujian Province (2024J08102 and 2023J02026); the National Natural Science Foundation of China (52302008, 22471271, and 52472015); the Self-deployment Project Research Program of Haixi Institutes Program, Chinese Academy of Science (CXZX-2022-GH06), the Youth Innovation Promotion Association CAS (Y2023082), and Fuzhou Science and Technology Program (2025-P-001).

References

1 H. S. Choi, J. Lin, G. Wang, W. P. D. Wong, I.-H. Park, F. Lin, J. Yin, K. Leng, J. H. Lin and K. P. Loh, Molecularly Thin, Two-Dimensional All-Organic Perovskites, *Science*, 2024, **384**, 60–66.
2 A. Jana, S. Cho, S. A. Patil, A. Meena, Y. Jo, V. G. Sree, Y. Park, H. Kim, H. Im and R. A. Taylor, Perovskite: Scintillators, Direct Detectors, and X-Ray Imagers, *Mater. Today*, 2022, **55**, 110–136.
3 Z. W. Xiao, Z. N. Song and Y. F. Yan, From Lead Halide Perovskites to Lead–Free Metal Halide Perovskites and Perovskite Derivatives, *Adv. Mater.*, 2019, **31**, 1803792.
4 Q. Y. Cui, S. F. Liu and K. Zhao, Structural and Functional Insights into Metal-Free Perovskites, *J. Phys. Chem. Lett.*, 2022, **13**, 5168–5178.

5 H. Chen, X. Chen, Z. Xu, H. Peng, Y. Qin, H. Lv, X. Song, S. Hu, L. Ji, J. Zhou, R. Xiong and W. Liao, A 3D Hybrid Perovskite Ferroelastic with Triclinic–to–Cubic Phase Transition Boosts Temperature/Pressure Dual On/Off Switchable Birefringence, *Angew. Chem., Int. Ed.*, 2025, **64**, e202503681.

6 L. A. Muscarella, G. Bravetti and J. V. Milić, The Emergence of Metal-Free Molecular Perovskites: Challenges and Opportunities, *Mater. Horiz.*, 2025, **12**, 6124–6132.

7 Y. J. Wu, Z. Z. Li, Y. T. Lei and Z. W. Jin, Metal–Free Perovskites for X–Ray Detection, *Chem. – Eur. J.*, 2023, **29**, e202301536.

8 H.-Y. Ye, Y.-Y. Tang, P.-F. Li, W.-Q. Liao, J.-X. Gao, X.-N. Hua, H. Cai, P.-P. Shi, Y.-M. You and R.-G. Xiong, Metal-Free Three-Dimensional Perovskite Ferroelectrics, *Science*, 2018, **361**, 151–155.

9 H. Zhang, Z.-K. Xu, Z.-X. Wang, H. Yu, H.-P. Lv, P.-F. Li, W.-Q. Liao and R.-G. Xiong, Large Piezoelectric Response in a Metal-Free Three-Dimensional Perovskite Ferroelectric, *J. Am. Chem. Soc.*, 2023, **145**, 4892–4899.

10 R. Z. Zhuang, X. J. Wang, W. B. Ma, Y. H. Wu, X. Chen, L. H. Tang, H. M. Zhu, J. Y. Liu, L. L. Wu, W. Zhou, X. Liu and Y. (Michael) Yang, Highly Sensitive X-Ray Detector Made of Layered Perovskite-like $(NH_4)_3Bi_2I_9$ Single Crystal with Anisotropic Response, *Nat. Photonics*, 2019, **13**, 602–608.

11 Y. Shang, R.-K. Huang, S.-L. Chen, C.-T. He, Z.-H. Yu, Z.-M. Ye, W.-X. Zhang and X.-M. Chen, Metal-Free Molecular Perovskite High-Energetic Materials, *Cryst. Growth Des.*, 2020, **20**, 1891–1897.

12 H. Morita, R. Tsunashima, S. Nishihara, K. Inoue, Y. Omura, Y. Suzuki, J. Kawamata, N. Hoshino and T. Akutagawa, Ferroelectric Behavior of a Hexamethylenetetramine–Based Molecular Perovskite Structure, *Angew. Chem., Int. Ed.*, 2019, **58**, 9184–9187.

13 J. Moriguchi, T. Koga, N. Tsunoji, S. Nishihara, T. Akutagawa, A. Masuya-Suzuki and R. Tsunashima, Solvent-Assisted Mechanochemical Crystallization of the Metal-Free Perovskite Solid Solution (H_2Dabco, H_2Hmta) $NH_4(BF_4)_3$, *Chem. Commun.*, 2024, **60**, 12181–12184.

14 Y. Gao, S. Meshkat, A. Johnston, C. Zheng, G. Walters, Q. X. Feng, X. P. Wang, M.-J. Sun, A. M. Najarian, D. J. Xue, Y.-K. Wang, M. I. Saidaminov, O. Voznyy, S. Hoogland and E. H. Sargent, Electro-Optic Modulation Using Metal-Free Perovskites, *ACS Appl. Mater. Interfaces*, 2021, **13**, 19042–19047.

15 J. Y. Fan, W. Li, Q. Zhou, G. Yang, P. F. Tang, J. H. He, L. Ma, J. F. Zhang, J. W. Xiao, Z. G. Yan, A. Li and X. D. Han, Metal Halide Perovskites for Direct X–Ray Detection in Medical Imaging: To Higher Performance, *Adv. Funct. Mater.*, 2025, **35**, 2401017.

16 H. D. Wu, Y. S. Ge, G. D. Niu and J. Tang, Metal Halide Perovskites for X-Ray Detection and Imaging, *Matter*, 2021, **4**, 144–163.

17 P. X. Dong, C. S. Lin, X. Zhao, Y. Lv, N. Ye and M. Luo, Synergistic Role of Hydrogen Bonding and Band Degeneracy Leads to Enhanced X-Ray Detection in HPIP-$(NH_4)_{0.7}Cs_{0.3}Br_3{\cdot}H_2O$ Perovskites, *Inorg. Chem. Front.*, 2024, **11**, 2709–2717.

18 Z. Z. Li, Z. H. Li, G. Q. Peng, C. Shi, H. X. Wang, S. Ding, Q. Wang, Z. T. Liu and Z. W. Jin, PF_6^- Pseudohalides Anion Based Metal–Free Perovskite Single Crystal for Stable X–Ray Detector to Attain Record Sensitivity, *Adv. Mater.*, 2023, **35**, 2300480.

19 Y. T. Lei, M. Y. Yin, C. Shi, L. X. Wu, G. Q. Peng, Y. K. Xu, H. X. Wang, R. B. Tang, Z. H. Li and Z. W. Jin, Tailored Molecular for Ultra-Stability and Biocompatible Pseudohalide Metal-Free Perovskite towards X-Ray Detectors with Record Sensitivity, *npj Flexible Electron.*, 2024, **8**, 46.

20 H. S. Choi, S. N. Li, I.-H. Park, W. H. Liew, Z. Y. Zhu, K. C. Kwon, L. Wang, I.-H. Oh, S. S. Zheng, C. L. Su, Q.-H. Xu, K. Yao, F. Pan and K. P. Loh, Tailoring the Coercive Field in Ferroelectric Metal-Free Perovskites by Hydrogen Bonding, *Nat. Commun.*, 2022, **13**, 794.

21 Z. Z. Li, G. Q. Peng, Z. H. Li, Y. K. Xu, T. Wang, H. X. Wang, Z. T. Liu, G. Wang, L. M. Ding and Z. W. Jin, Hydrogen Bonds Strengthened Metal–Free Perovskite for Degradable X–ray Detector with Enhanced Stability, Flexibility and Sensitivity, *Angew. Chem., Int. Ed.*, 2023, **62**, e202218349.

22 L.-L. Chu, T. Zhang, W.-Y. Zhang, P.-P. Shi, J.-X. Gao, Q. Ye and D.-W. Fu, Three-Dimensional Metal-Free Molecular Perovskite with a Thermally Induced Switchable Dielectric Response, *J. Phys. Chem. Lett.*, 2020, **11**, 1668–1674.

23 G. Q. Peng, Z. H. Li, Y. K. Xu, Y. T. Lei, H. X. Wang and Z. W. Jin, Evidence of Cation Symmetry Reduction Induced Bulk Photovoltaic Effect in Metal–Free Perovskite for Efficient Self–Powered X–Ray Detection, *Adv. Mater.*, 2025, **37**, 2502335.

24 T. S. Li, S. L. Luo, X. J. Wang and L. J. Zhang, Alternative Lone–Pair Ns^2–Cation–Based Semiconductors beyond Lead Halide Perovskites for Optoelectronic Applications, *Adv. Mater.*, 2021, **33**, 2008574.

25 Z. Guo, J. W. Lin and L. L. Mao, Dynamic Control of Halide Perovskite Structures for Tailored Ferroelectric and Second-Order Nonlinear Optical Functionalities, *Chem. Soc. Rev.*, 2025, **54**, 8845–8887.

26 Q. Y. Cui, X. M. Liu, N. Li, H. Q. Zeng, D. P. Chu, H. J. Li, X. Song, Z. Xu, Y. P. Liu, H. M. Zhu, K. Zhao and S. Liu, A New Metal–Free Molecular Perovskite–Related Single Crystal with Quantum Wire Structure for High–Performance X–Ray Detection, *Small*, 2024, **20**, 2308945.

27 X. Song, H. Cohen, J. Yin, H. J. Li, J. Y. Wang, Y. Y. Yuan, R. W. Huang, Q. Y. Cui and C. Ma, S. (Frank) Liu, G. Hodes and K. Zhao, Low Dimensional, Metal–Free, Hydrazinium Halide Perovskite–Related Single Crystals and Their Use as X–Ray Detectors, *Small*, 2023, **19**, 2300892.

28 P. Dong, C. Lin, N. Ye and M. Luo, Dimensional Regulation in Metal–Free Perovskites by Compositional Engineering to

Achieve Record Low X–Ray Detection Limits, *Angew. Chem., Int. Ed.*, 2024, **63**, e202407048.

29 H. Li, X. Song, C. Ma, Z. Xu, N. Bu, T. Yang, Q. Cui, L. Gao, Z. Yang, F. Gao, G. Zhao, Z. Chen, Z. Ding, K. Zhao and S. (Frank) Liu, Lead-Free Molecular One-Dimensional Perovskite for Efficient X-Ray Detection, *J. Energy Chem.*, 2022, **64**, 209–213.

30 W. Li, M. Li, Y. He, J. Song, K. Guo, W. Pan and H. Wei, Arising 2D Perovskites for Ionizing Radiation Detection, *Adv. Mater.*, 2024, **36**, 2309588.

31 Z. Li, S. Shi, G. Peng, Y. Wu, H. Xie, H. Wang, Z. Li and Z. Jin, Metal-Free Hydrazinium Halide Perovskitoid Single Crystals for X-Ray Detection, *Nano Lett.*, 2023, **23**, 9972–9979.

32 K. B. Zheng and T. Pullerits, Two Dimensions Are Better for Perovskites, *J. Phys. Chem. Lett.*, 2019, **10**, 5881–5885.

33 G.-Z. Liu, J. Zhang and L.-Y. Wang, A Novel Molecular Cubic Perovskite Built From Charge-Assisted Hydrogen Bond Linkages, *Synth. React. Inorg., Met.-Org., Nano-Met. Chem.*, 2011, **41**, 1091–1094.

34 H. J. Li, T. L. Li, C. Ma, X. M. Liu, L. Lang, T. H. Yang, X. Song, Q. Y. Cui, Z. Yang, S. (Frank) Liu and K. Zhao, "One–Click Restart" Recycling of Metal–Free Perovskite X–Ray Detectors, *Adv. Mater.*, 2024, **36**, 2400783.

35 Z. Z. Li, Y. Q. Pang, G. Q. Peng, H. X. Wang, Q. J. Li, X. F. Zhou, Z. H. Li, Q. Wang and Z. W. Jin, Aminoazanium of A-Site Cations in Metal-Free Halide Perovskite Single Crystals to Reduce Thermal Expansion for Efficient X-Ray Detection, *J. Phys. Chem. Lett.*, 2024, **15**, 4375–4383.

36 L. J. Wei, Y. Liu, Y. Ma, Q. S. Fan, L. W. Tang, J. T. Zhang, J. H. Luo and Z. H. Sun, Centimeter-Level Double Perovskite Single Crystals with Strong Interlaminar Hydrogen Bonds for High-Performance X-Ray Detection, *J. Mater. Chem. C*, 2025, **13**, 1675–1679.

37 Q. S. Fan, H. J. Xu, Z. Zhu, Z. H. Zhao, H. Rong, P. F. Zhu, W. Q. Guo, L. W. Tang, J. T. Zhang, J. H. Luo and Z. H. Sun, 3D Lead–Free Double Perovskite via Anchoring A–Site Cation for Ultralow Dose and Stable X–Ray Detection, *Adv. Funct. Mater.*, 2025, **35**, 2505546.

38 C. H. Deng, S. H. You, J. S. Xie, Z. Zhou, Q. W. Guan, H. Q. Zhong, J. B. Wu, Y. J. Zhao and W. Q. Yang, A One-Dimensional Lead-Free Hybrid Perovskite for Stable X-Ray Detection with Low Detection Limits, *J. Mater. Chem. A*, 2025, **13**, 27417–27424.

39 Y. P. Fan, Q. Chen, Z. Li, T. T. Zhu, J. B. Wu, S. H. You, S. H. Zhang, J. H. Luo and C. M. Ji, Realization of Passive X–Ray Detection with a Low Detection Limit in Dion–Jacobson Halide Hybrid Perovskite, *Small*, 2023, **19**, 2303814.

40 Q. W. Guan, S. H. You, Z. Zhu, R. Q. Li, H. Ye, C. S. Zhang, H. Li, C. M. Ji, X. T. Liu and J. H. Luo, Three–Dimensional Polar Perovskites for Highly Sensitive Self–Driven X–Ray Detection, *Angew. Chem., Int. Ed.*, 2024, **63**, e202320180.

41 H. Li, Y. Wu, Q. W. Guan, C. M. Ji, H. Ye, Z. Y. Wu, S. Chen, C. S. Zhang, Y. Li, H. Liu and J. H. Luo, Bimetallic Co–Occupation and Multiple Interlayer Interactions in Aromatic Double Perovskite for Highly Sensitive and Stable Self–Driven X–Ray Detection, *Adv. Mater.*, 2026, **38**, e11539.

42 Y. T. Lei, G. Q. Peng, Z. Guan, Y. K. Xu, H. X. Wang, H. Xie, Z. H. Li and Z. W. Jin, Synergistic Rare–Earth Alloying and Pseudohalide Coordination Constructing Hybrid Metal Pseudohalide with Robust Crystal Fields for Stable X–Ray Detection with Record Sensitivity, *Adv. Funct. Mater.*, 2026, **36**, e15738.

43 T. Y. Shi, W. J. Liu, J. T. Zhu, X. S. Fan, Z. Y. Zhang, X. C. He, R. He, J. H. Wang, K. Z. Chen, Y. S. Ge, X. M. Sun, Y. L. Liu, P. K. Chu and X.-F. Yu, $CsPbBr_3$-DMSO Merged Perovskite Micro-Bricks for Efficient X-Ray Detection, *Nano Res.*, 2023, **16**, 9983–9989.

44 Z. Z. Li, G. Q. Peng, H. Y. Chen, C. Shi, Z. H. Li and Z. W. Jin, Metal-Free PAZE-$NH_4X_3{\cdot}H_2O$ Perovskite for Flexible Transparent X–ray Detection and Imaging, *Angew. Chem., Int. Ed.*, 2022, **61**, e202207198.

45 J. Chen, L. Tang, C. Gong, L. Wei, J. Zhang, X. Chen, X. Zhang, Y. Liu, J. Luo and Z. Sun, Improper narrow bandgap molecular ferroelectrics enable light-excited pyroelectricity for broadband self-powered photoactivities, *Inorg. Chem. Front.*, 2026, **13**, 86–94.

46 Z. Li, Y. Wang and Z. Jin, Metal-Free Perovskites for X-Ray Detection and imaging: Progress and Prospects, *EcoEnergy*, 2025, **3**, e70013.

47 CCDC 2528731: Experimental Crystal Structure Determination, 2026, DOI: **10.5517/ccdc.csd.cc2qwbzy**.

